
Generative Models as Distributions of Functions

Emilien Dupont¹ Yee Whye Teh¹ Arnaud Doucet¹

Abstract

Generative models are typically trained on grid-like data such as images. As a result, the size of these models usually scales directly with the underlying grid resolution. In this paper, we abandon discretized grids and instead parameterize individual data points by continuous functions. We then build generative models by learning distributions over such functions. By treating data points as functions, we can abstract away from the specific type of data we train on and construct models that scale independently of signal resolution and dimension. To train our model, we use an adversarial approach with a discriminator that acts directly on continuous signals. Through experiments on both images and 3D shapes, we demonstrate that our model can learn rich distributions of functions independently of data type and resolution.

1. Introduction

In generative modeling, data is often represented by discrete arrays. Images are represented by two dimensional grids of RGB values, 3D scenes are represented by three dimensional voxel grids and audio as vectors of discretely sampled waveforms. However, it is often the case that the true underlying signal is continuous. We can therefore also consider representing such signals by continuous functions taking as input grid coordinates and returning features. In the case of images for example, we can define a function $f : \mathbb{R}^2 \rightarrow \mathbb{R}^3$ mapping pixel locations to RGB values. Such representations, typically referred to as implicit neural representations, coordinate-based neural representations or neural function representations, have the remarkable property that they are independent of signal resolution (Park et al., 2019; Mescheder et al., 2018; Chen & Zhang, 2019; Sitzmann et al., 2020).

In this paper, we build generative models that inherit the attractive properties of implicit representations. By framing generative modeling as learning distributions of functions, we are able to build models that act entirely on continuous

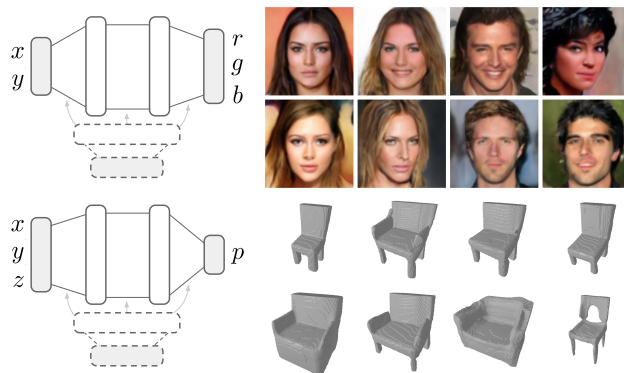


Figure 1. By representing data as continuous functions, we can use the same model to learn distributions of images and 3D shapes.

spaces, independently of resolution. We achieve this by parameterizing a distribution over neural networks with a hypernetwork (Ha et al., 2017) and training this distribution with an adversarial approach (Goodfellow et al., 2014). Crucially, by expressing all our data in terms of coordinates and features and introducing a discriminator that acts entirely on point clouds, we can train the model irrespective of any underlying discretization or grid. This approach also allows us to abstract away from the specific type of data we train on. Indeed, our method applies as long as we can express our data in terms of coordinates and features and define a notion of distance on the coordinate space.

To validate our approach, we train generative models on various image and 3D shape datasets. Remarkably, we show that, using our framework, we can learn rich function distributions on both images and 3D shapes using the *same model*. Further, by taking advantage of recent advances in representing high frequency functions with neural networks (Mildenhall et al., 2020; Tancik et al., 2020; Sitzmann et al., 2020), we also show that, unlike current approaches for generative modeling on continuous spaces (Park et al., 2019; Garnele et al., 2018a), we are able to generate sharp and realistic samples. Finally, we explore the continuity of the learned representations and show that our model is often able to generate plausible samples at higher resolutions than it was trained on.

In summary, we make the following contributions:

- We introduce a novel class of generative models where

¹University of Oxford. Correspondence to: Emilien Dupont <dupont@stats.ox.ac.uk>.

data is represented as a function parameterized by a neural network. We generate data by sampling the neural network weights from a learned distribution and probing the resulting function at the desired locations.

- We develop a training procedure that is independent of data resolution and only requires the availability of a sensible metric on the domain of the neural functions.
- We demonstrate, through experiments, that we can use the same model to learn rich function distributions on both image and 3D shape datasets.

2. Representing data as a function

For clarity, we use the case of representing an image by a function as a guiding example, but the methods described here hold for much more general data (see Section 2.2).

2.1. Representing a single image with a function

Let I be an image such that $I[x, y]$ corresponds to the RGB value at pixel location (x, y) . We are interested in representing this image by a function $f : \mathbb{R}^2 \rightarrow \mathbb{R}^3$ where $f(x, y) = (r, g, b)$ returns the RGB values at pixel location (x, y) . To achieve this, we parameterize a function f_θ by an MLP with weights θ . We can then learn the function representation by minimizing

$$\min_{\theta} \sum_{x,y} \|f_\theta(x, y) - I[x, y]\|_2^2,$$

where the sum is over all pixel locations. Remarkably, the representation f_θ is *independent* of the number of pixels. The representation f_θ therefore, unlike most image representations, does not depend on the resolution of the image.

2.2. Representing general data with a function

The above example with images can readily be extended to more general data. Let $\mathbf{x} \in \mathbb{R}^d$ denote coordinates and $\mathbf{y} \in \mathbb{R}^k$ features and assume we are given a data point as a set of coordinate and feature pairs $\{(\mathbf{x}_i, \mathbf{y}_i)\}_{i=1}^n$. For an image for example, $\mathbf{x} = (x, y)$ corresponds to pixel locations, $\mathbf{y} = (r, g, b)$ corresponds to RGB values and $\{(\mathbf{x}_i, \mathbf{y}_i)\}_{i=1}^n$ to the set of all pixel locations and RGB values. Given a set of coordinates and their corresponding features, we can then consider learning a function $f_\theta : \mathbb{R}^d \rightarrow \mathbb{R}^k$ representing this data point by minimizing

$$\min_{\theta} \sum_{i=1}^n \|f_\theta(\mathbf{x}_i) - \mathbf{y}_i\|_2^2. \quad (1)$$

For function representations, the only assumption on the data is that it can be expressed in terms of coordinates and features. This is very general and includes:

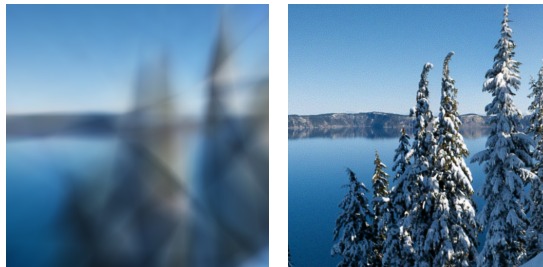


Figure 2. Modeling an image with a function with (right) and without (left) a Fourier feature encoding. Without Fourier features, the function is unable to represent high frequency detail.

- Images: $f : \mathbb{R}^2 \rightarrow \mathbb{R}^3, f(x, y) = (r, g, b)$.
- Videos: $f : \mathbb{R}^3 \rightarrow \mathbb{R}^3, f(x, y, t) = (r, g, b)$.
- Voxels: $f : \mathbb{R}^3 \rightarrow \{0, 1\}, f(x, y, z) = p$ where $p = 0$ for an empty voxel and $p = 1$ for an occupied voxel.

The core property of these representations is that they scale with signal *complexity* and not with signal resolution (Sitzmann et al., 2020). Indeed, the memory required to store data scales quadratically with resolution for images and cubically for voxel grids. In contrast, for function representations, the memory requirements scale directly with signal complexity: to represent a more complex signal, we would need to increase the capacity of the function f_θ , for example by increasing the number of layers in the case of a neural network. This scaling is often much better than the quadratic or cubic scaling required for typical discrete grid representations (Park et al., 2019).

2.3. Representing high frequency functions

Recently, it has been shown that learning function representations by minimizing equation (1) is biased towards learning low frequency functions (Mildenhall et al., 2020; Sitzmann et al., 2020; Tancik et al., 2020). To alleviate this problem, several approaches have been proposed. Mildenhall et al. (2020) transform the coordinates \mathbf{x} with a sinusoidal encoding layer before passing it through the network f_θ . Sitzmann et al. (2020) propose learning MLPs with sinusoidal activations and Tancik et al. (2020) use random Fourier features (Rahimi & Recht, 2008) on the coordinates. In this paper, we use the random Fourier feature (RFF) encoding as it is not biased towards on axis variation (unlike Mildenhall et al. (2020)) and does not require specialized initialization (unlike Sitzmann et al. (2020)). Specifically, given a coordinate $\mathbf{x} \in \mathbb{R}^d$, the encoding function $\gamma : \mathbb{R}^d \rightarrow \mathbb{R}^{2m}$ is defined as

$$\gamma(\mathbf{x}) = \begin{pmatrix} \cos(2\pi B\mathbf{x}) \\ \sin(2\pi B\mathbf{x}) \end{pmatrix},$$

where $B \in \mathbb{R}^{m \times d}$ is a (potentially learnable) random matrix whose entries are typically sampled from $\mathcal{N}(0, \sigma^2)$. The

number of frequencies m and the variance σ^2 of the entries of B are hyperparameters. To learn high frequency functions, we simply encode \mathbf{x} before passing it through the MLP and minimize

$$\min_{\theta} \sum_{i=1}^n \|f_{\theta}(\gamma(\mathbf{x}_i)) - \mathbf{y}_i\|_2^2.$$

As can be seen in Figure 2, learning a function representation of an image with a ReLU MLP fails to capture high frequency detail whereas using an RFF encoding allows us to faithfully reproduce the image.

3. Learning distributions of functions

In generative modeling, we are typically given a set of data, such as images, and are interested in approximating the distribution of this data. As we represent data points by functions, we would therefore like to learn a distribution over functions. In the case of images, standard generative models typically sample some noise and feed it through a neural network to output n pixels (Goodfellow et al., 2014; Kingma & Welling, 2013; Rezende et al., 2014). In contrast, we sample the weights of a neural network to obtain a function which we can probe at arbitrary coordinates. Such a representation allows us to operate entirely on coordinates and features irrespective of any underlying grid representation that may be available.

To train the function distribution we use an adversarial approach. While it is possible to use other methods, we favored adversarial training as generative adversarial networks (GAN) are typically able to generate sharp and high frequency samples (Karras et al., 2017; 2019).

3.1. Neural function distributions

In this section, we describe how to parameterize a distribution over functions. We assume the structure (e.g. the number and width of layers) of the MLP f_{θ} representing a single data point is fixed. Learning a distribution over functions f_{θ} is then equivalent to learning a distribution over weights $p(\theta)$. The distribution $p(\theta)$ is defined by a latent distribution $p(\mathbf{z})$ and a second function $g_{\phi} : \mathcal{Z} \rightarrow \Theta$, itself with parameters ϕ , mapping latent variables to the weights θ of f_{θ} (see Figure 3). We can then sample from $p(\theta)$ by sampling $\mathbf{z} \sim p(\mathbf{z})$ and mapping \mathbf{z} through g_{ϕ} to obtain a set of weights $\theta = g_{\phi}(\mathbf{z})$. We refer to such a distribution over functions as a neural function distribution (NFD).

Note that the function g_{ϕ} is itself a neural network parameterizing the weights of another neural network f_{θ} and as such is a hypernetwork (Ha et al., 2017). Hypernetworks, and special cases thereof (Sitzmann et al., 2020), have been extensively used to parameterize spaces of 3D scenes (Park et al., 2019; Mescheder et al., 2019; Sitzmann et al., 2019).

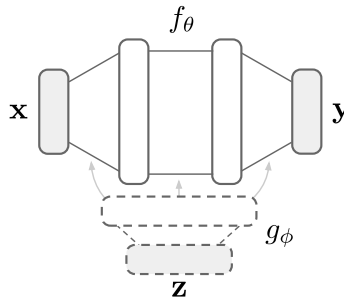


Figure 3. Diagram of neural function distribution architecture. A latent vector \mathbf{z} is mapped through a hypernetwork g_{ϕ} (in dashed lines) to obtain the weights of a function f_{θ} (in solid lines) mapping coordinates \mathbf{x} to features \mathbf{y} .

3.2. Data representation

As implicit representations define functions from arbitrary coordinates to arbitrary features, we would like NFDs to operate purely on coordinates and features too. As such, we assume our data is given in terms of coordinates \mathbf{x} and features \mathbf{y} . A single data point then corresponds to a set of coordinates and features $\mathbf{s} = \{(\mathbf{x}_i, \mathbf{y}_i)\}_{i=1}^n$. We then assume a dataset is given to us as samples $\mathbf{s} \sim p(\mathbf{s})$ from a distribution over sets of coordinate and feature pairs.

Indeed, while our goal is to learn a distribution over functions, we typically do not have access to the ground truth functions representing the data (e.g. we do not have access to a function mapping pixel locations to RGB values for a real image). However, we do have access to input/output pairs of these functions through the coordinates and features, allowing us to learn function distributions without operating directly on the functions.

Crucially, formulating our problem entirely on sets lets us split individual data points into subsets and train on those. Specifically, given a single data point $\mathbf{s} = \{s_1, s_2, \dots, s_n\}$, we can randomly subsample K elements to create a subset $\mathbf{s}_K = \{s_{i_1}, s_{i_2}, \dots, s_{i_K}\}$ (e.g. for an image, we can select K pixels among the n pixels in the entire image). Learning on such subsets effectively corresponds to performing stochastic gradient descent by splitting *individual data points* into batches and not only splitting the training dataset into batches of data points. Training on such subsets also removes any dependence on the resolution n of the data.

3.3. Function generator

Learning distributions of functions with an adversarial approach requires us to define a generator that generates fake functions and a discriminator that distinguishes between real and fake functions. We define the generator with an NFD and use functions generated from this distribution to generate fake sets of coordinate and feature pairs. Specifically, the fake data generation follows two steps: 1. sample

a function f_θ from an NFD, 2. evaluate f_θ at a set of coordinates $\{\mathbf{x}_i\}$ to obtain a set of generated features $\{\mathbf{y}_i\}$. Specifically, given a latent vector \mathbf{z} and a coordinate \mathbf{x}_i , we compute a generated feature as $\mathbf{y}_i = f_{g_\phi(\mathbf{z})}(\gamma(\mathbf{x}_i))$ where γ is an RFF encoding allowing us to learn high frequency functions. As these operations are all differentiable, we can obtain gradients with respect to ϕ to train the model.

3.4. Point cloud discriminator

In the GAN literature, discriminators are almost always parameterized with convolutional neural networks (CNN). However, the data we consider may not necessarily lie on a grid, in which case it is not possible to use convolutional discriminators. Further, convolutional discriminators scale directly with grid resolution (training a CNN on images at $2\times$ the resolution requires $4\times$ the memory) which partially defeats the purpose of using implicit representations.

As the core idea of our paper is to build generative models that are independent of resolution, we therefore cannot follow the naive approach of using convolutional discriminators. Instead, our discriminator should be able to distinguish between real and fake sets of coordinate and feature pairs. Specifically, we need to define a function D which takes in an *unordered set* \mathbf{s} and returns the probability that this set represents input/output pairs of a real function. We therefore need D to be permutation invariant with respect to the elements s_i of the set $\mathbf{s} = \{s_1, s_2, \dots, s_n\}$.

The canonical choice for set functions is the PointNet (Qi et al., 2017a) or DeepSets (Zaheer et al., 2017) model family. However, we experimented extensively with such functions and found that they were not adequate for learning complex function distributions (see Section 3.6 for further details). Indeed, while the input to the discriminator is an unordered set $\mathbf{s} = \{(\mathbf{x}_i, \mathbf{y}_i)\}$, there is an underlying notion of distance between points \mathbf{x}_i in the coordinate space. We found that it is crucial to take this into account when training models on large scale datasets. Indeed, we should not consider the coordinate and feature pairs as sets but rather as *point clouds* (i.e. sets with an underlying notion of distance).

3.4.1. POINTCONV

While several works have tackled the problem of point cloud classification (Qi et al., 2017a; Li et al., 2018; Thomas et al., 2019), we leverage the PointConv framework introduced by Wu et al. (2019) for several reasons. Firstly, PointConv layers are translation equivariant (like regular convolutions) and permutation invariant by construction. Secondly, when sampled on a regular grid, PointConv networks closely match the performance of regular CNNs. Indeed, we can loosely think of PointConv as a continuous equivalent of CNNs and, as such, we can build PointConv architectures that are analogous to typical discriminator architectures.

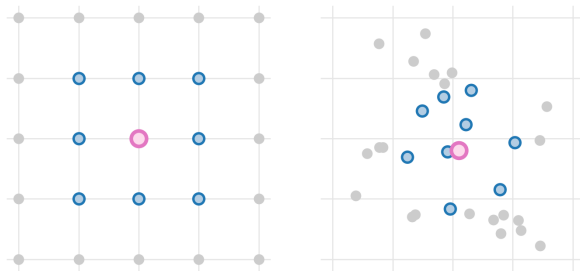


Figure 4. Convolution neighborhood for regular convolutions (left) and PointConv (right). Regular convolutions are defined on a grid while PointConv is defined on continuous spaces and finds the nearest neighbors (in some metric) to a given query point and performs a convolution with these.

Specifically, we assume we are given a set of features $\mathbf{f}_i \in \mathbb{R}^{c_{in}}$ at locations \mathbf{x}_i (we use \mathbf{f}_i to distinguish these hidden features of the network from input features \mathbf{y}_i). In contrast to regular convolutions, where the convolution kernels are only defined at certain grid locations, the convolution filters in PointConv are parameterized by an MLP, $W : \mathbb{R}^d \rightarrow \mathbb{R}^{c_{out} \times c_{in}}$, mapping coordinates to kernel values. We can therefore evaluate the convolution filters in the entire coordinate space. The PointConv operation¹ at a point \mathbf{x} is then defined as

$$\mathbf{f}_{out}(\mathbf{x}) = \sum_{\mathbf{x}_i \in N_{\mathbf{x}}} W(\mathbf{x}_i - \mathbf{x})\mathbf{f}_i,$$

where $N_{\mathbf{x}}$ is a set of neighbors over which to perform the convolution (see Figure 4). Interestingly, this neighborhood is found by a nearest neighbor search with respect to some metric on the coordinate space. We therefore have more flexibility in defining the convolution operation as we can choose the most appropriate notion of distance for the space we want to model (our implementation supports fast computation on the GPU for any ℓ_p norm). While the neighborhood used for standard convolutions on the grid corresponds to the ℓ_∞ norm, we use the ℓ_2 norm in our experiments.

Another key operation in CNNs is downsampling such as pooling and strided convolutions. For images for example, we can perform average pooling by averaging features over groups of 4 pixels, effectively reducing the number of pixels by a factor of 4. We can define analogous operations in the continuous case by sampling a number of query points from the input point cloud (e.g. sampling 1/4 of the points for an image) and using these as centers for either convolution or pooling operations over a neighborhood of points (again in a metric of our choice). We found that simply using convolutions followed by average pooling layers allowed us to learn rich function distributions with point cloud discriminators.

¹Computing this operation naively is expensive, but Wu et al. (2019) introduce a trick to reduce this significantly by reordering sums

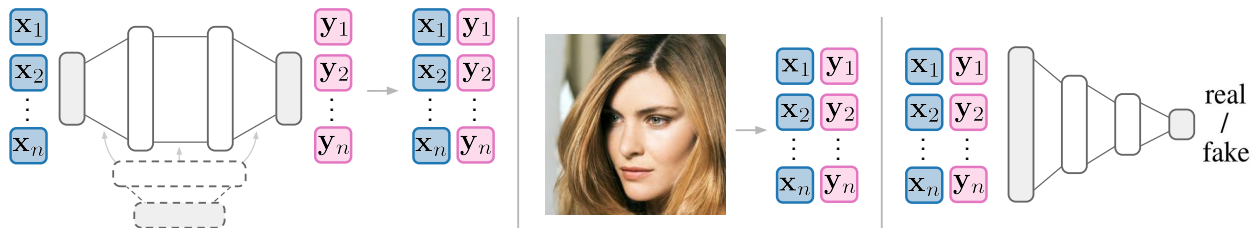


Figure 5. Training procedure for neural function distributions: 1. Sample a function from NFD and evaluate it at various coordinate locations to generate fake point cloud. 2. Convert real data sample to point cloud. 3. Discriminate between real and fake point clouds.

3.5. Training

We use the traditional (non saturating) GAN loss (Goodfellow et al., 2014) for training and illustrate the entire procedure for a single training step in Figure 5. To stabilize training, we define an equivalent for point clouds of the R_1 penalty from Mescheder et al. (2018). For images, R_1 regularization corresponds to penalizing the gradient norm of the discriminator with respect to the input image. For a set $\mathbf{s} = \{(\mathbf{x}_i, \mathbf{y}_i)\}_{i=1}^n$, we define the penalty as

$$R_1(\mathbf{s}) = \frac{1}{2} \|\nabla_{\mathbf{y}_1, \dots, \mathbf{y}_n} D(\mathbf{s})\|^2 = \frac{1}{2} \sum_{\mathbf{y}_i} \|\nabla_{\mathbf{y}_i} D(\mathbf{s})\|^2,$$

that is we penalize the gradient norm of the discriminator with respect to the features. Using R_1 regularization was not strictly necessary for our models to converge but we found that it gave slight but consistent improvements in performance. Crucially, our entire modeling procedure is then independent of the resolution n . Indeed, the generator, discriminator and loss all act on point clouds which can be subsampled independently of resolution.

3.6. How not to learn distributions of functions

In developing our model, we found that several approaches which intuitively seem appropriate for learning distributions of functions do not work in the context of generative modeling. We briefly describe these here and provide further details and proofs in the appendix.

Set discriminators. As described in Section 3.4, the canonical choice for set functions is the PointNet/DeepSet model family (Qi et al., 2017a; Zaheer et al., 2017). However, we found both theoretically and experimentally that these functions were not suitable as discriminators for complex function distributions. Indeed, these models do not directly take advantage of the metric on the space of coordinates, which we conjecture is crucial for learning rich function distributions. In addition, we show in the appendix that the Lipschitz constant of set functions can be very large, leading to unstable GAN training (Arjovsky et al., 2017; Roth et al., 2017; Mescheder et al., 2018). We provide further theoretical and experimental insights on the use of set functions as discriminators in the appendix.

Auto-decoders. A common method for embedding functions into a latent space is the auto-decoder framework (Park et al., 2019). This framework and variants of it have been extensively used in 3D computer vision (Park et al., 2019; Sitzmann et al., 2019). While auto-decoders excel at a variety of tasks, we show in the appendix that the objective used to train these models is not appropriate for generative modeling. We provide further analysis and experimental results on auto-decoders in the appendix.

While none of the above models were able to learn function distributions on complex datasets such as CelebA HQ, all of them worked well on MNIST. We therefore believe that MNIST is not a meaningful benchmark for generative modeling of functions and encourage future research in this area to include experiments on more complex datasets.

4. Related work

Implicit representations. Implicit representations for 3D geometry were initially (and concurrently) proposed by (Park et al., 2019; Mescheder et al., 2019; Chen & Zhang, 2019). A large body of work has since taken advantage of these representations for inverse rendering (Sitzmann et al., 2019; Mildenhall et al., 2020; Niemeyer et al., 2020; Yu et al., 2020), modeling dynamic scenes (Niemeyer et al., 2019; Pumarola et al., 2020), modeling 3D scenes (Atzmon & Lipman, 2020; Jiang et al., 2020; Gropp et al., 2020) and superresolution (Chen & Zhang, 2019). As implicit representations are biased towards low frequency functions, Mildenhall et al. (2020) proposed using a positional encoding to learn high frequency representations. This has since been extended to MLPs with sinusoidal activation functions (Sitzmann et al., 2020) as well as random Fourier features (Tancik et al., 2020).

Distributions of functions. A large portion of work on implicit representations focuses on representing single instances but some of these have also been applied to distributions of representations (Park et al., 2019; Mescheder et al., 2019; Sitzmann et al., 2019; 2020). While these models are able to embed data into a space of implicit representations, they typically do not learn distributions from which we can sample and as such are not suitable for generative

modeling. Neural processes (Garnelo et al., 2018a;b) are another family of models that learn distributions of functions. However, the focus of these is on uncertainty quantification and meta-learning rather than generative modeling. Further, these models do not scale to large datasets, although adding attention (Kim et al., 2019) and translation equivariance (Gordon et al., 2019) helps alleviate this. In concurrent work, Skorokhodov et al. (2020); Anokhin et al. (2020); Chan et al. (2020) have also used an adversarial approach to learn distributions of high frequency implicit representations. However, these works use standard convolutional grid discriminators and as such do not inherit several advantages of implicit representations: they are restricted to images lying on a grid and scale directly with the number of pixels. In contrast, our model is entirely continuous and independent of resolution and, as a result, we are able to train on a variety of datasets with limited computational resources.

Point clouds. Since the introduction of PointNet (Qi et al., 2017a), several works have used pointwise MLPs with an aggregation function to extract features from point clouds (Qi et al., 2017b; Zhao et al., 2019; Yan et al., 2020). Other methods are based on building equivalents of grid convolutions for point clouds, including parameterizing convolution filters by MLPs (Liu et al., 2019b;a; Wu et al., 2019), using learnable kernel points or products of simple functions (Xu et al., 2018; Thomas et al., 2019) or applying continuous transformations before performing convolutions (Li et al., 2018). For a complete survey of point cloud methods in deep learning we refer the reader to Guo et al. (2020).

5. Experiments

We evaluate our model on CelebAHQ (Karras et al., 2017) at 64×64 and 128×128 resolution as well as on 3D shapes from the ShapeNet (Chang et al., 2015) chairs category. Note that for both images and 3D shapes we use the *exact same model* except for the input and output dimensions of the function representation and the hyperparameters of the Fourier features. For all datasets, we use an MLP with 3 hidden layers of size 128 for the function representation and an MLP with 2 hidden layers of size 256 and 512 for the hypernetwork parameterizing the NFD. Remarkably, we find that such a simple architecture is sufficient for learning rich distributions of images and 3D shapes.

The point cloud discriminator is loosely based on the the DCGAN architecture (Radford et al., 2015) with layers that get wider as the number of points decreases. More specifically, we use 3^d neighbors for each PointConv layer and downsample points by a factor of 2^d at every pooling layer while doubling the number of channels. We implemented our model in PyTorch (Paszke et al., 2019) and performed all training on a single 2080Ti GPU with 11GB of RAM. For additional experimental details, please refer to the appendix.



Figure 6. Samples from our model trained on CelebAHQ 64×64 (top) and 128×128 (bottom). Each image corresponds to a function which was sampled from our model and then evaluated on the grid. To produce this figure we sampled 5 batches and chose the best batch by visual inspection.

5.1. Generative modeling

We first evaluate our model on the task of image generation. To generate images, we sample a function from the learned NFD and evaluate it on a grid. As can be seen in in Figure 6, our model produces sharp and realistic images both at 64×64 and 128×128 resolution. While there are still artifacts and occasionally poor samples (particularly at 128×128 resolution), the images are generally convincing and show that the model has learned a meaningful distribution of functions representing the data. To the best of our knowledge, this is the first time data of this complexity has been modeled in an entirely continuous fashion.

5.2. Superresolution

As the representations we learn are independent of resolution, we can use our model to generate images at higher resolutions than the data on which it was trained. We show examples of this in Figure 7 by first sampling a function from our model, evaluating it at the resolution on which it was trained and then evaluating it at a $4\times$ higher resolution. Surprisingly, our model is able to generate convincing and reasonably sharp images at 256×256 resolution even though it has only ever seen 64×64 images during training. Further, the inductive bias from the Fourier features and coordinate-based representations results in sharper and higher quality images than when using bicubic upsampling.

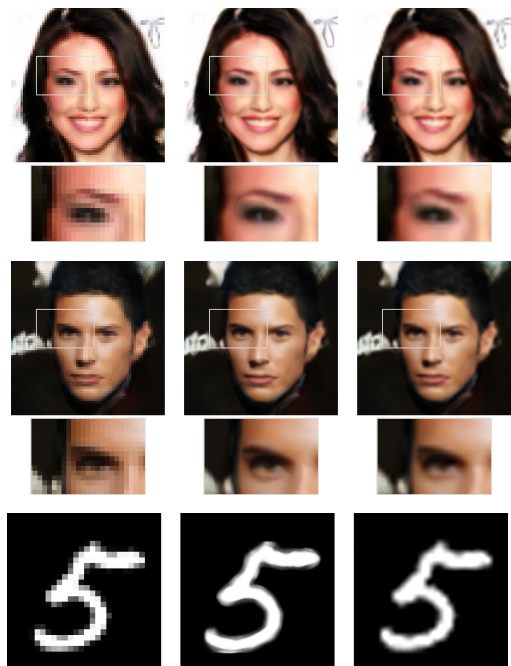


Figure 7. Examples of superresolution. Each row corresponds to a function sampled from our model. The first column corresponds to the function evaluated at 64×64 (28×28 for MNIST) resolution and the second column to the function evaluated at 256×256 resolution. The third column shows the result of bicubic upsampling on the first column to match the resolution of the second.

5.3. Baselines

In this section we compare our model against three baselines: a model trained using the auto-decoder framework (Park et al., 2019), a model trained with a set discriminator and a convolutional neural process (ConvNP) (Gordon et al., 2019). To the best of our knowledge, these are the only other model families that can learn generative models in a continuous manner, without relying on a grid representation (which is required for regular CNNs). While there are several models in the neural process family, we compare against ConvNPs as these are the best performing variant and also allow for unconditional sampling². Results comparing all three models on CelebAHQ 32×32 are shown in Figure 8. As can be seen, the auto-decoder model generates blurry and incoherent samples. The set discriminator model generates samples with wave-like artifacts and the ConvNP model produces blurry samples with little diversity. In contrast, our model is able to generate sharp, diverse and plausible samples. Further, as shown in Section 5.1, our model generates coherent samples well beyond the 32×32 resolution considered here.

²Note that the main task of ConvNPs is to generate images based on a context set and it may be possible to improve unconditional sampling by changing the way context sets are sampled.

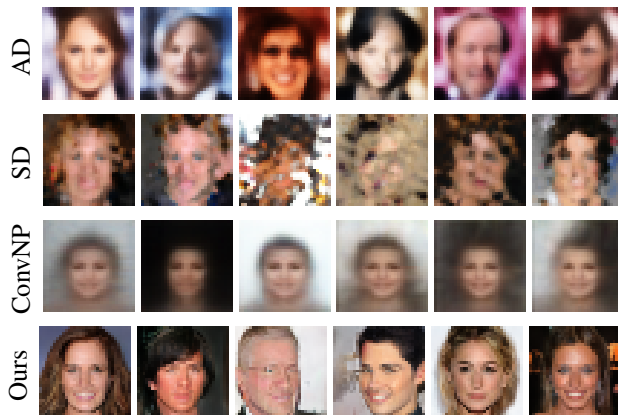


Figure 8. Baseline comparisons on CelebAHQ 32×32 . AD refers to an auto-decoder, SD to a set discriminator and ConvNP to a convolutional neural process. Note that the ConvNP model was trained on CelebA (not CelebAHQ) and as such has a different crop than the other models.

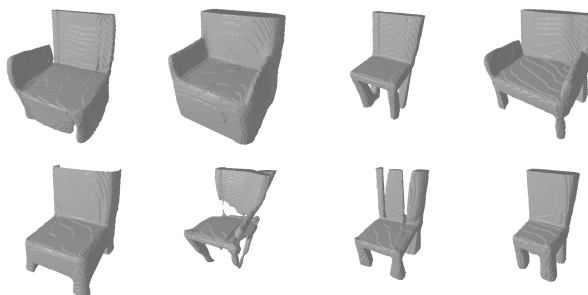


Figure 9. Samples from our model trained on ShapeNet chairs. While the model was trained on 32^3 data, the generated samples are at 128^3 resolution. To generate the plot, we sampled 5 batches and chose the best batch by visual inspection.

5.4. 3D scenes

To test the versatility of our model, we also train it on a different task: generating 3D shapes. To achieve this, we let the function representation $f_\theta : \mathbb{R}^3 \rightarrow \mathbb{R}$ map x, y, z coordinates to an occupancy probability p (which is 0 if the location is empty and 1 if it is part of an object). To generate data, we follow the setup from Mescheder et al. (2019). Specifically, we use the voxel grids from Choy et al. (2016) representing the chairs category from the ShapeNet (Chang et al., 2015) dataset. The dataset contains 6778 chairs each of dimension 32^3 . As each 3D model corresponds to a set of $32^3 = 32,768$ points, we uniformly subsample $K = 4096$ points from each object and feed those to the model during training. Surprisingly, even though the model only sees partial representations of the objects, we are able to learn plausible distributions of complete objects.

In order to visualize results, we convert the continuous functions sampled from our model to meshes we can render. To achieve this, we first sample a function from our model and evaluate it on a high resolution grid (usually 128^3).

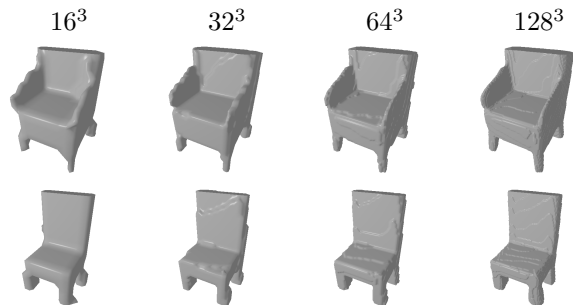


Figure 10. Evaluating the same function at different resolutions. As samples from our model can be probed at arbitrary coordinates, we can increase the resolution to render smoother meshes.

We then threshold the values of this grid at 0.5 (we found the model was robust to choices of threshold) so voxels with values above the threshold are occupied while the rest are empty. Finally, we use the marching cubes algorithm (Lorenson & Cline, 1987) to convert the grid to a 3D mesh which we render with PyTorch3D (Ravi et al., 2020).

Samples from our model are shown in Figure 9. As can be seen our model is able to generate mostly coherent and realistic samples. The continuous nature of the data representation also allows us to sample our model at high resolutions to produce clean and smooth surfaces (see Figure 10). Remarkably, we were able to use the same model we used for images with little tuning or hyperparameter searches.

6. Scope, limitations and future work

Limitations. One of the main weaknesses of our method is that it does not match the sample quality of state of the art convolutional generative models (Karras et al., 2019; 2020). While the goal of this paper was not to create state of the art samples but rather to demonstrate that we can learn rich data distributions in function space, it would still be desirable to narrow the gap in performance. We strived for simplicity when designing our model but hypothesize that approaches such as progressive growing (Karras et al., 2017), using specialized generator architectures (Karras et al., 2019) and losses (Arjovsky et al., 2017), truncating the prior distribution (Brock et al., 2018) and using residual connections in the discriminator could help improve sample quality. We include failure examples in Figure 11.

Another weakness of our model is that determining the neighborhood for the point cloud convolution can be slow when a large number of points is used. Running such nearest neighbor searches typically becomes prohibitively slow beyond 32k points. Finding alternative architectures or incorporating methods for fast neighbor search is therefore an important direction of future work (Johnson et al., 2019).

In addition, we found that subsampling the point cloud typically leads to less stable training. For example, on

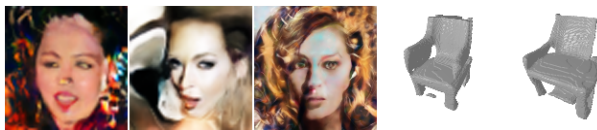


Figure 11. Failure examples of unrealistic and incoherent samples.

CelebAHQ, decreasing the number of points per example also decreases the quality of the generated images. We conjecture that this is due to the nearest neighbor search in the discriminator: when subsampling points, a nearest neighbor may lie very far from a query point, potentially leading to unstable training. More refined sampling methods (such as sampling patches instead of sampling uniformly) as well as radius neighborhood searches (which have been shown to be more robust than nearest neighbor searches (Thomas et al., 2019)) should help improve stability.

Future work. We believe there are many interesting avenues for future work. Firstly, as our model only depends on coordinates and features and a notion of distance on the coordinate space, it would be interesting to extend our model to more exotic spaces and manifolds. In addition, it would be interesting to apply our model to geospatial (Jean et al., 2016), geological (Dupont et al., 2018), meteorological (Sønderby et al., 2020) or molecular (Wu et al., 2018) data which typically doesn't lie on a regular grid.

In computer vision, we hope that our approach will help scale generative models to larger datasets. While our model in its current form could not scale to truly large datasets (such as room scale 3D scenes or very high resolution images), framing generative models entirely in terms of coordinates and features could be a first step towards this (Sitzmann et al., 2020). It would also be interesting to incorporate symmetries into our model (Finzi et al., 2020) either for inverse rendering (Dupont et al., 2020) or for scene generation. For example, the realism of a point cloud does not depend on the pose in which it is observed and as such the discriminator should be rotation and translation invariant.

Finally, while we have trained our model using an adversarial approach it would also be interesting explore other methods for learning distributions independently of resolution. For example, it would be interesting to train our model using variational inference with a point cloud posterior.

7. Conclusion

In this paper, we introduced a method for learning generative models that act entirely on continuous spaces and as such are independent of signal resolution. We achieved this by learning distributions over functions representing the data instead of learning distributions over the data directly. Through experiments on both images and 3D shapes, we showed that our model learns rich function distributions independently of the underlying data type and resolution.

8. Acknowledgements

We thank William Zhang, Yuyang Shi, Jin Xu, Valentin De Bortoli, Jean-Francois Ton and Kaspar Märtens for providing feedback on an early version of the paper. We also thank Charline Le Lan, Jean-Francois Ton and Bobby He for helpful discussions. We thank Yann Dubois for providing the ConvNP samples as well as helpful discussions around neural processes. Emilien gratefully acknowledges his PhD funding from Google DeepMind.

References

- Anokhin, I., Demochkin, K., Khakhulin, T., Sterkin, G., Lempitsky, V., and Korzhenkov, D. Image generators with conditionally-independent pixel synthesis. *arXiv preprint arXiv:2011.13775*, 2020.
- Arjovsky, M., Chintala, S., and Bottou, L. Wasserstein generative adversarial networks. In *Proceedings of the 34th International Conference on Machine Learning-Volume 70*, pp. 214–223, 2017.
- Atzmon, M. and Lipman, Y. Sal: Sign agnostic learning of shapes from raw data. In *Proceedings of the IEEE/CVF Conference on Computer Vision and Pattern Recognition*, pp. 2565–2574, 2020.
- Brock, A., Donahue, J., and Simonyan, K. Large scale gan training for high fidelity natural image synthesis. *arXiv preprint arXiv:1809.11096*, 2018.
- Chan, E. R., Monteiro, M., Kellnhofer, P., Wu, J., and Wetzstein, G. pi-gan: Periodic implicit generative adversarial networks for 3d-aware image synthesis. *arXiv preprint arXiv:2012.00926*, 2020.
- Chang, A. X., Funkhouser, T., Guibas, L., Hanrahan, P., Huang, Q., Li, Z., Savarese, S., Savva, M., Song, S., Su, H., et al. Shapenet: An information-rich 3d model repository. *arXiv preprint arXiv:1512.03012*, 2015.
- Chen, Z. and Zhang, H. Learning implicit fields for generative shape modeling. In *Proceedings of the IEEE/CVF Conference on Computer Vision and Pattern Recognition*, pp. 5939–5948, 2019.
- Choy, C. B., Xu, D., Gwak, J., Chen, K., and Savarese, S. 3d-r2n2: A unified approach for single and multi-view 3d object reconstruction. In *European conference on computer vision*, pp. 628–644. Springer, 2016.
- Dupont, E., Zhang, T., Tilke, P., Liang, L., and Bailey, W. Generating realistic geology conditioned on physical measurements with generative adversarial networks. *arXiv preprint arXiv:1802.03065*, 2018.
- Dupont, E., Martin, M. B., Colburn, A., Sankar, A., Susskind, J., and Shan, Q. Equivariant neural rendering. In *International Conference on Machine Learning*, pp. 2761–2770. PMLR, 2020.
- Finzi, M., Stanton, S., Izmailov, P., and Wilson, A. G. Generalizing convolutional neural networks for equivariance to lie groups on arbitrary continuous data. In *International Conference on Machine Learning*, pp. 3165–3176. PMLR, 2020.
- Garnelo, M., Rosenbaum, D., Maddison, C., Ramalho, T., Saxton, D., Shanahan, M., Teh, Y. W., Rezende, D., and Eslami, S. A. Conditional neural processes. In *International Conference on Machine Learning*, pp. 1704–1713. PMLR, 2018a.
- Garnelo, M., Schwarz, J., Rosenbaum, D., Viola, F., Rezende, D. J., Eslami, S., and Teh, Y. W. Neural processes. *arXiv preprint arXiv:1807.01622*, 2018b.
- Goodfellow, I. J., Pouget-Abadie, J., Mirza, M., Xu, B., Warde-Farley, D., Ozair, S., Courville, A., and Bengio, Y. Generative adversarial networks. *arXiv preprint arXiv:1406.2661*, 2014.
- Gordon, J., Bruinsma, W. P., Foong, A. Y., Requeima, J., Dubois, Y., and Turner, R. E. Convolutional conditional neural processes. *arXiv preprint arXiv:1910.13556*, 2019.
- Gropp, A., Yariv, L., Haim, N., Atzmon, M., and Lipman, Y. Implicit geometric regularization for learning shapes. *arXiv preprint arXiv:2002.10099*, 2020.
- Gulrajani, I., Ahmed, F., Arjovsky, M., Dumoulin, V., and Courville, A. C. Improved training of Wasserstein gans. In *Advances in Neural Information Processing Systems*, pp. 5767–5777, 2017.
- Guo, Y., Wang, H., Hu, Q., Liu, H., Liu, L., and Bennamoun, M. Deep learning for 3d point clouds: A survey. *IEEE transactions on pattern analysis and machine intelligence*, 2020.
- Ha, D., Dai, A., and Le, Q. V. HyperNetworks. *International Conference on Learning Representations*, 2017.
- Ioffe, S. and Szegedy, C. Batch normalization: Accelerating deep network training by reducing internal covariate shift. In *International conference on machine learning*, pp. 448–456. PMLR, 2015.
- Jean, N., Burke, M., Xie, M., Davis, W. M., Lobell, D. B., and Ermon, S. Combining satellite imagery and machine learning to predict poverty. *Science*, 353(6301):790–794, 2016.

- Jiang, C., Sud, A., Makadia, A., Huang, J., Nießner, M., Funkhouser, T., et al. Local implicit grid representations for 3d scenes. In *Proceedings of the IEEE/CVF Conference on Computer Vision and Pattern Recognition*, pp. 6001–6010, 2020.
- Johnson, J., Douze, M., and Jégou, H. Billion-scale similarity search with GPUs. *IEEE Transactions on Big Data*, 2019.
- Karras, T., Aila, T., Laine, S., and Lehtinen, J. Progressive growing of gans for improved quality, stability, and variation. *arXiv preprint arXiv:1710.10196*, 2017.
- Karras, T., Laine, S., and Aila, T. A style-based generator architecture for generative adversarial networks. In *Proceedings of the IEEE/CVF Conference on Computer Vision and Pattern Recognition*, pp. 4401–4410, 2019.
- Karras, T., Laine, S., Aittala, M., Hellsten, J., Lehtinen, J., and Aila, T. Analyzing and improving the image quality of stylegan. In *Proceedings of the IEEE/CVF Conference on Computer Vision and Pattern Recognition*, pp. 8110–8119, 2020.
- Kim, H., Mnih, A., Schwarz, J., Garnelo, M., Eslami, A., Rosenbaum, D., Vinyals, O., and Teh, Y. W. Attentive neural processes. *arXiv preprint arXiv:1901.05761*, 2019.
- Kingma, D. P. and Welling, M. Auto-encoding variational Bayes. *arXiv preprint arXiv:1312.6114*, 2013.
- Lee, J., Lee, Y., Kim, J., Kosiorek, A., Choi, S., and Teh, Y. W. Set transformer: A framework for attention-based permutation-invariant neural networks. In *International Conference on Machine Learning*, pp. 3744–3753. PMLR, 2019.
- Li, Y., Bu, R., Sun, M., Wu, W., Di, X., and Chen, B. Pointcnn: Convolution on x-transformed points. *Advances in neural information processing systems*, 31:820–830, 2018.
- Liu, Y., Fan, B., Meng, G., Lu, J., Xiang, S., and Pan, C. Densepoint: Learning densely contextual representation for efficient point cloud processing. In *Proceedings of the IEEE/CVF International Conference on Computer Vision*, pp. 5239–5248, 2019a.
- Liu, Y., Fan, B., Xiang, S., and Pan, C. Relation-shape convolutional neural network for point cloud analysis. In *Proceedings of the IEEE/CVF Conference on Computer Vision and Pattern Recognition*, pp. 8895–8904, 2019b.
- Lorensen, W. E. and Cline, H. E. Marching cubes: A high resolution 3d surface construction algorithm. *ACM SIGGRAPH computer graphics*, 21(4):163–169, 1987.
- Mescheder, L., Geiger, A., and Nowozin, S. Which training methods for gans do actually converge? In *International Conference on Machine Learning (ICML)*, pp. 3481–3490. PMLR, 2018.
- Mescheder, L., Oechsle, M., Niemeyer, M., Nowozin, S., and Geiger, A. Occupancy networks: Learning 3d reconstruction in function space. In *Proceedings of the IEEE/CVF Conference on Computer Vision and Pattern Recognition*, pp. 4460–4470, 2019.
- Mildenhall, B., Srinivasan, P. P., Tancik, M., Barron, J. T., Ramamoorthi, R., and Ng, R. Nerf: Representing scenes as neural radiance fields for view synthesis. *arXiv preprint arXiv:2003.08934*, 2020.
- Miyato, T., Kataoka, T., Koyama, M., and Yoshida, Y. Spectral normalization for generative adversarial networks. In *International Conference on Learning Representations*, 2018.
- Niemeyer, M., Mescheder, L., Oechsle, M., and Geiger, A. Occupancy flow: 4d reconstruction by learning particle dynamics. In *Proceedings of the IEEE/CVF International Conference on Computer Vision*, pp. 5379–5389, 2019.
- Niemeyer, M., Mescheder, L., Oechsle, M., and Geiger, A. Differentiable volumetric rendering: Learning implicit 3d representations without 3d supervision. In *Proc. IEEE Conf. on Computer Vision and Pattern Recognition (CVPR)*, 2020.
- Park, J. J., Florence, P., Straub, J., Newcombe, R., and Lovegrove, S. Deepsdf: Learning continuous signed distance functions for shape representation. In *Proceedings of the IEEE Conference on Computer Vision and Pattern Recognition*, pp. 165–174, 2019.
- Paszke, A., Gross, S., Massa, F., Lerer, A., Bradbury, J., Chanan, G., Killeen, T., Lin, Z., Gimelshein, N., Antiga, L., et al. Pytorch: An imperative style, high-performance deep learning library. *arXiv preprint arXiv:1912.01703*, 2019.
- Pumarola, A., Corona, E., Pons-Moll, G., and Moreno-Noguer, F. D-nerf: Neural radiance fields for dynamic scenes. *arXiv preprint arXiv:2011.13961*, 2020.
- Qi, C. R., Su, H., Mo, K., and Guibas, L. J. Pointnet: Deep learning on point sets for 3d classification and segmentation. In *Proceedings of the IEEE conference on Computer Vision and Pattern Recognition*, pp. 652–660, 2017a.
- Qi, C. R., Yi, L., Su, H., and Guibas, L. J. Pointnet++: Deep hierarchical feature learning on point sets in a metric space. *arXiv preprint arXiv:1706.02413*, 2017b.

- Radford, A., Metz, L., and Chintala, S. Unsupervised representation learning with deep convolutional generative adversarial networks. *arXiv preprint arXiv:1511.06434*, 2015.
- Rahimi, A. and Recht, B. Random features for large-scale kernel machines. In *Advances in neural information processing systems*, pp. 1177–1184, 2008.
- Ravi, N., Reizenstein, J., Novotny, D., Gordon, T., Lo, W.-Y., Johnson, J., and Gkioxari, G. Accelerating 3d deep learning with pytorch3d. *arXiv preprint arXiv:2007.08501*, 2020.
- Rezende, D. J., Mohamed, S., and Wierstra, D. Stochastic backpropagation and approximate inference in deep generative models. In *International conference on machine learning*, pp. 1278–1286. PMLR, 2014.
- Roth, K., Lucchi, A., Nowozin, S., and Hofmann, T. Stabilizing training of generative adversarial networks through regularization. In *Advances in neural information processing systems*, pp. 2018–2028, 2017.
- Sitzmann, V., Zollhöfer, M., and Wetzstein, G. Scene representation networks: Continuous 3d-structure-aware neural scene representations. In *Advances in Neural Information Processing Systems*, pp. 1121–1132, 2019.
- Sitzmann, V., Martel, J. N., Bergman, A. W., Lindell, D. B., and Wetzstein, G. Implicit neural representations with periodic activation functions. *arXiv preprint arXiv:2006.09661*, 2020.
- Skorokhodov, I., Ignatyev, S., and Elhoseiny, M. Adversarial generation of continuous images. *arXiv preprint arXiv:2011.12026*, 2020.
- Sønderby, C. K., Espeholt, L., Heek, J., Dehghani, M., Oliver, A., Salimans, T., Agrawal, S., Hickey, J., and Kalchbrenner, N. Metnet: A neural weather model for precipitation forecasting. *arXiv preprint arXiv:2003.12140*, 2020.
- Tancik, M., Srinivasan, P. P., Mildenhall, B., Fridovich-Keil, S., Raghavan, N., Singhal, U., Ramamoorthi, R., Barron, J. T., and Ng, R. Fourier features let networks learn high frequency functions in low dimensional domains. *arXiv preprint arXiv:2006.10739*, 2020.
- Thomas, H., Qi, C. R., Deschaud, J.-E., Marcotegui, B., Goulette, F., and Guibas, L. J. Kpconv: Flexible and deformable convolution for point clouds. In *Proceedings of the IEEE/CVF International Conference on Computer Vision*, pp. 6411–6420, 2019.
- Wu, W., Qi, Z., and Fuxin, L. Pointconv: Deep convolutional networks on 3d point clouds. In *Proceedings of the IEEE Conference on Computer Vision and Pattern Recognition*, pp. 9621–9630, 2019.
- Wu, Z., Ramsundar, B., Feinberg, E. N., Gomes, J., Geniesse, C., Pappu, A. S., Leswing, K., and Pande, V. Moleculenet: a benchmark for molecular machine learning. *Chemical Science*, 9(2):513–530, 2018.
- Xu, Y., Fan, T., Xu, M., Zeng, L., and Qiao, Y. Spidercnn: Deep learning on point sets with parameterized convolutional filters. In *Proceedings of the European Conference on Computer Vision (ECCV)*, pp. 87–102, 2018.
- Yan, X., Zheng, C., Li, Z., Wang, S., and Cui, S. Pointasnl: Robust point clouds processing using nonlocal neural networks with adaptive sampling. In *Proceedings of the IEEE/CVF Conference on Computer Vision and Pattern Recognition*, pp. 5589–5598, 2020.
- Yu, A., Ye, V., Tancik, M., and Kanazawa, A. pixelnerf: Neural radiance fields from one or few images. *arXiv preprint arXiv:2012.02190*, 2020.
- Zaheer, M., Kottur, S., Ravanbakhsh, S., Póczos, B., Salakhutdinov, R. R., and Smola, A. J. Deep sets. In *Advances in Neural Information Processing Systems*, pp. 3391–3401, 2017.
- Zhao, H., Jiang, L., Fu, C.-W., and Jia, J. Pointweb: Enhancing local neighborhood features for point cloud processing. In *Proceedings of the IEEE/CVF Conference on Computer Vision and Pattern Recognition*, pp. 5565–5573, 2019.

A. Experimental details

In this section we provide experimental details necessary to reproduce all results in the paper. All the models were implemented in PyTorch (Paszke et al., 2019) and trained on a single 2080Ti GPU with 11GB of RAM.

A.1. Single image experiment

To produce Figure 2, we trained a ReLU MLP with 2 hidden layers each with 256 units, using tanh as the final non-linearity. We trained for 1000 iterations with Adam using a learning rate of 1e-3. For the RFF encoding we set $m = 256$ and $\sigma = 10$.

A.2. Distribution experiments

For all experiments (both images and 3D shapes), we parameterized f_θ by an MLP with 3 hidden layers, each with 128 units. We used a latent dimension of 64 and an MLP with 2 hidden layers of dimension 256 and 512 for the hypernetwork g_ϕ . We normalized all coordinates to lie in $[-1, 1]^d$ and all features to lie in $[-1, 1]^k$. We used LeakyReLU non-linearities both in the NFD and discriminator. The final output of the function representation was followed by a tanh non-linearity.

For the point cloud discriminator, we used 3^d neighbors in each convolution layer and followed every convolution by an average pooling layer reducing the number of points by 2^d . We applied a sigmoid as the final non-linearity. We used an MLP with 4 hidden layers each of size 16 to parameterize all weight MLPs. Unless stated otherwise, we use Adam with a learning rate of 1e-4 for the hypernetwork weights and 4e-4 for the discriminator weights with $\beta_1 = 0.5$ and $\beta_2 = 0.999$ as is standard for GAN training. For each dataset, we trained for a large number of epochs and chose the best model by visual inspection.

A.2.1. MNIST

- Dimensions: $d = 2, k = 1$
- Fourier features: $m = 128, \sigma = 1$
- Discriminator channels: 64, 128, 256
- Batch size: 128
- Epochs: 150

A.2.2. CELEBAHQ 64x64

- Dimensions: $d = 2, k = 3$
- Fourier features: $m = 128, \sigma = 2$
- Discriminator channels: 64, 128, 256, 512
- Batch size: 64
- Epochs: 300

A.2.3. CELEBAHQ 128x128

- Dimensions: $d = 2, k = 3$
- Fourier features: $m = 128, \sigma = 3$
- Discriminator channels: 64, 128, 256, 512, 1024
- Batch size: 22
- Epochs: 70

A.2.4. SHAPENET CHAIRS

- Dimensions: $d = 3, k = 1$
- Fourier features: None
- Discriminator channels: 64, 128, 256
- Batch size: 24
- Learning rates: Generator 2e-5, Discriminator 8e-5
- Epochs: 200

A.2.5. THINGS WE TRIED THAT DIDN'T WORK

- We initially let the function representation f_θ have 2 hidden layers of size 256, instead of 3 layers of size 128. However, we found that this did not work well, particularly for more complex datasets. We hypothesize that this is because the number of weights in a single $256 \rightarrow 256$ linear layer is $4\times$ the number of weights in a single $128 \rightarrow 128$ layer. As such, the number of weights in four $128 \rightarrow 128$ layers is the same as a single $256 \rightarrow 256$, even though such a 4-layer network would be much more expressive. Since the hypernetwork needs to output all the weights of the function representation, the final layer of the hypernetwork will be extremely large if the number of function weights is large. It is therefore important to make the network as expressive as possible with as few weights as possible, i.e. by making the network thinner and deeper.
- As the paper introducing the R_1 penalty (Mescheder et al., 2018) does not use batchnorm (Ioffe & Szegedy, 2015) in the discriminator, we initially ran experiments without using batchnorm. However, we found that using batchnorm both in the weight MLPs and between PointConv layers was crucial for stable training. We hypothesize that this is because using standard initializations for the weights of PointConv layers would result in PointConv outputs (which correspond to the weights in regular convolutions) that are large. Adding batchnorm fixed this initialization issue and resulted in stable training.
- In the PointConv paper, it was shown that the number of hidden layers in the weight MLPs does not significantly affect classification performance (Wu et al., 2019). We therefore initially experimented with single hidden layer MLPs for the weights. However, we found that it is crucial to use deep networks for the weight MLPs in order to build discriminators that are expressive enough for the datasets we consider.
- We experimented with learning the frequencies of the Fourier features (i.e. learning B) but found that this did not significantly boost performance and generally resulted in slower training.

B. Models that are not suitable for learning function distributions

B.1. Auto-decoders

We briefly introduce auto-decoder models following the setup in (Park et al., 2019) and describe why they are not suitable as generative models. As in the NFD case, we assume we are given a dataset of N samples $\{\mathbf{s}^{(i)}\}_{i=1}^N$ (where each sample $\mathbf{s}^{(i)}$ is a set). We then associate a latent vector $\mathbf{z}^{(i)}$ with each sample $\mathbf{s}^{(i)}$. We further parameterize a probabilistic model $p_\theta(\mathbf{s}^{(i)}|\mathbf{z}^{(i)})$ (similar to the decoder in variational autoencoders) by a neural network with learnable parameters θ (typically returning the mean of a Gaussian with fixed variance). The optimal parameters are then estimated as

$$\arg \max_{\theta, \{\mathbf{z}^{(i)}\}} \sum_{i=1}^N \log p_\theta(\mathbf{s}^{(i)}|\mathbf{z}^{(i)}) + \log p(\mathbf{z}^{(i)}),$$

where $p(\mathbf{z})$ is a (typically Gaussian) prior over the $\mathbf{z}^{(i)}$'s. Crucially the latent vectors $\mathbf{z}^{(i)}$ are themselves learnable and optimized. However, maximizing $\log p(\mathbf{z}^{(i)}) \propto -\|\mathbf{z}^{(i)}\|^2$ does not encourage the $\mathbf{z}^{(i)}$'s to be distributed according to the prior, but only encourages them to have a small norm. Note that this is because we are optimizing the *samples* and not the *parameters* of the Gaussian prior. As such, after training, the $\mathbf{z}^{(i)}$'s are unlikely to be distributed according to the prior. Sampling from the prior to generate new samples from the model will therefore not work.



Figure 12. Left: Samples from an auto-decoder model trained on MNIST. Right: Samples from an auto-decoder model trained on CelebAHQ 32×32 .

We hypothesize that this is why the prior is required to have very low variance for the auto-decoder model to work well (Park et al., 2019). Indeed, if the norm of the $\mathbf{z}^{(i)}$'s is so small that they are barely changed during training, they will remain close to their initial Gaussian distribution. While this trick is sufficient to learn distributions of simple datasets such as MNIST, we were unable to obtain good results on more complex and high frequency datasets such as CelebAHQ. Results of our best models are shown in Figure 12.

We also note that auto-decoders were not necessarily built to act as generative models. Auto-decoders have for example excelled at embedding 3D shape data into a latent space (Park et al., 2019) and learning distributions over 3D scenes for inverse rendering (Sitzmann et al., 2019). Our analysis therefore does not detract from the usefulness of auto-decoders, but instead shows that auto-decoders may not be suitable for the task of generative modeling.

B.2. Set discriminators

In this section, we analyse the use of set discriminators for learning NFDs. Given a datapoint $\mathbf{s} = \{(\mathbf{x}_i, \mathbf{y}_i)\}_{i=1}^n$ represented as a set, we build a permutation invariant set discriminator as a PointNet/DeepSet (Qi et al., 2017a; Zaheer et al., 2017) function

$$D(\mathbf{s}) = \rho \left(\frac{1}{\sqrt{n}} \sum_{i=1}^n \varphi(\gamma_x(\mathbf{x}_i), \gamma_y(\mathbf{y}_i)) \right),$$

where ρ and φ are both MLPs and γ_x and γ_y are RFF encodings for the coordinates and features respectively. Recall that the RFF encoding function γ is defined as

$$\gamma(\mathbf{x}) = \begin{pmatrix} \cos(2\pi B\mathbf{x}) \\ \sin(2\pi B\mathbf{x}) \end{pmatrix},$$

where B is a (potentially learnable) random matrix of frequencies. While the RFF encodings are not strictly necessary, we were unable to learn high frequency functions without them. Note also that we normalize the sum over set elements by \sqrt{n} instead of n as is typical - as shown in Section B.3.1 this is to make the Lipschitz constant of the set discriminator independent of n .

We experimented extensively with such models, varying architectures and encoding hyperparameters (including not using an encoding) but were unable to get satisfactory results on CelebAHQ, even at a resolution of 32×32 . Our best results are shown in Figure 13. As can be seen, the model is able to generate plausible samples for MNIST but fails on CelebAHQ.

While PointNet/DeepSet functions are universal approximators of set functions (Zaheer et al., 2017), they do not explicitly model set element interactions. As such, we also experimented with Set Transformers (Lee et al., 2019) which model interactions using self-attention. However, we found that using such architectures did not improve performance. As mentioned in the main paper, we therefore conjecture that explicitly taking into account the metric on the coordinate space (as is done in PointConv) is crucial for learning complex neural distributions.

In addition to our experimental results, we also provide some theoretical evidence that set discriminators may be ill-suited for generative modeling of functions. Specifically, we show that the Lipschitz constant of set discriminators and RFF encodings are typically very large.



Figure 13. Left: Samples from a set discriminator model trained on MNIST. Right: Samples from a set discriminator model trained on CelebAHQ 32×32 .

B.3. The Lipschitz constant of set discriminators

Several works have shown that limiting the Lipschitz constant (or equivalently the largest gradient norm) of the discriminator is important for stable GAN training (Arjovsky et al., 2017; Gulrajani et al., 2017; Roth et al., 2017; Miyato et al., 2018; Mescheder et al., 2018). This is typically achieved either by penalizing the gradient norm or by explicitly constraining the Lipschitz constant of each layer in the discriminator. Intuitively, this ensures that the gradients of the discriminator with respect to its input do not grow too large and hence that gradients with respect to the weights of the generator do not grow too large either (which can lead to unstable training). In the following subsections, we show that the Lipschitz constant of set discriminators and specifically the Lipschitz constant of RFF encodings are large in most realistic settings.

B.3.1. ARCHITECTURE

Proposition 1. *The Lipschitz constant of the set discriminator D is bounded by*

$$\text{Lip}(D) \leq \text{Lip}(\rho)\text{Lip}(\varphi)\sqrt{\text{Lip}(\gamma_x)^2 + \text{Lip}(\gamma_y)^2}$$

See Section C for a proof. In the case where the RFF encoding is fixed, imposing gradient penalties on D would therefore reduce the Lipschitz constant of ρ and φ but not of γ_x and γ_y . If the RFF encoding is learned, its Lipschitz constant could also be penalized. However, as shown in (Tancik et al., 2020), learning high frequency functions typically requires large frequencies in the matrix B . We show in the following section that the Lipschitz constant of γ is directly proportional to the spectral norm of B .

B.3.2. LIPSCHITZ CONSTANT OF RANDOM FOURIER FEATURES

Proposition 2. *The Lipschitz constant of $\gamma(\mathbf{x})$ is bounded by*

$$\text{Lip}(\gamma) \leq \sqrt{8\pi}\|B\|$$

See Section C for a proof. There is therefore a fundamental tradeoff between how much high frequency detail the discriminator can learn (requiring a large Lipschitz constant) and its training stability (requiring a low Lipschitz constant). In practice, for the settings we used in this paper, the spectral norm of B is on the order of 100s, which is too large for stable GAN training.

C. Proofs

C.1. Prerequisites

We denote by $\|\cdot\|_2$ the ℓ_2 norm for vectors and by $\|\cdot\|$ the spectral norm for matrices (i.e. the matrix norm induced by the ℓ_2 norm). The spectral norm is defined as

$$\|A\| = \sup_{\|\mathbf{x}\|_2=1} \|A\mathbf{x}\|_2 = \sigma_{\max}(A) = \sqrt{\lambda_{\max}(A^T A)}$$

where σ_{\max} denotes the largest singular value and λ_{\max} the largest eigenvalue.

For a function $f : \mathbb{R}^n \rightarrow \mathbb{R}^m$, the Lipschitz constant $\text{Lip}(f)$ (if it exists) is defined as the largest value L such that

$$\|f(\mathbf{x}_1) - f(\mathbf{x}_2)\|_2 \leq L\|\mathbf{x}_1 - \mathbf{x}_2\|_2$$

for all $\mathbf{x}_1, \mathbf{x}_2$. The Lipschitz constant is equivalently defined for differentiable functions as

$$\text{Lip}(f) = \sup_{\mathbf{x}} \|\nabla f(\mathbf{x})\|.$$

Note that when composing two functions f and g we have

$$\text{Lip}(f \circ g) \leq \text{Lip}(f)\text{Lip}(g).$$

We will also make use of the following lemmas.

C.1.1. SPECTRAL NORM OF CONCATENATION

Lemma 1. Let $A \in \mathbb{R}^{n \times d}$ and $B \in \mathbb{R}^{m \times d}$ be two matrices and denote by $\begin{pmatrix} A \\ B \end{pmatrix}$ their rowwise concatenation. Then we have the following inequality in the spectral norm

$$\left\| \begin{pmatrix} A \\ B \end{pmatrix} \right\| \leq \sqrt{\|A\|^2 + \|B\|^2}.$$

*Proof.*³

$$\begin{aligned} \left\| \begin{pmatrix} A \\ B \end{pmatrix} \right\|^2 &= \lambda_{\max} \left(\begin{pmatrix} A \\ B \end{pmatrix}^T \begin{pmatrix} A \\ B \end{pmatrix} \right) \\ &= \lambda_{\max}(A^T A + B^T B) \\ &\leq \lambda_{\max}(A^T A) + \lambda_{\max}(B^T B) \\ &= \|A\|^2 + \|B\|^2, \end{aligned}$$

where we used the definition of the spectral norm in the first line and Weyl's inequality for symmetric matrices in the third line.

C.1.2. INEQUALITY FOR ℓ_1 AND ℓ_2 NORM

Lemma 2. Let $\mathbf{x}_i \in \mathbb{R}^d$ for $i = 1, \dots, n$. Then

$$\sum_{i=1}^n \|\mathbf{x}_i\|_2 \leq \sqrt{n} \|(\mathbf{x}_1, \dots, \mathbf{x}_n)\|_2.$$

Proof.

$$\begin{aligned} \sum_{i=1}^n \|\mathbf{x}_i\|_2 &= \sum_{i=1}^n \|\mathbf{x}_i\|_2 \cdot 1 \\ &\leq \left(\sum_{i=1}^n \|\mathbf{x}_i\|_2^2 \right)^{\frac{1}{2}} \left(\sum_{i=1}^n 1^2 \right)^{\frac{1}{2}} \\ &= \sqrt{n} \|(\mathbf{x}_1, \dots, \mathbf{x}_n)\|_2, \end{aligned}$$

where we used Cauchy-Schwarz in the second line. Note that this is an extension of the well-known inequality $\|\mathbf{x}\|_1 \leq \sqrt{n}\|\mathbf{x}\|_2$ to the case where each component of the vector \mathbf{x} is the ℓ_2 norm of another vector.

³This proof was inspired by <https://math.stackexchange.com/questions/2006773/spectral-norm-of-concatenation-of-two-matrices>

C.1.3. LIPSCHITZ CONSTANT OF SUM OF IDENTICAL FUNCTIONS

Lemma 3. Let $\mathbf{x}_i \in \mathbb{R}^d$ for $i = 1, \dots, n$ and let f be a function with Lipschitz constant $\text{Lip}(f)$. Define $g(\mathbf{x}_1, \dots, \mathbf{x}_n) = \sum_{i=1}^n f(\mathbf{x}_i)$. Then

$$\text{Lip}(g) \leq \sqrt{n}\text{Lip}(f).$$

Proof.

$$\begin{aligned} \|g(\mathbf{x}_1, \dots, \mathbf{x}_n) - g(\mathbf{y}_1, \dots, \mathbf{y}_n)\|_2 &= \left\| \sum_{i=1}^n (f(\mathbf{x}_i) - f(\mathbf{y}_i)) \right\|_2 \\ &\leq \sum_{i=1}^n \|f(\mathbf{x}_i) - f(\mathbf{y}_i)\|_2 \\ &\leq \text{Lip}(f) \sum_{i=1}^n \|\mathbf{x}_i - \mathbf{y}_i\|_2 \\ &\leq \sqrt{n}\text{Lip}(f) \left\| \begin{pmatrix} \mathbf{x}_1 \\ \vdots \\ \mathbf{x}_n \end{pmatrix} - \begin{pmatrix} \mathbf{y}_1 \\ \vdots \\ \mathbf{y}_n \end{pmatrix} \right\|_2. \end{aligned}$$

Where we used the triangle inequality for norms in the second line, the definition of Lipschitz constants in the second line and Lemma 2 in the third line.

C.1.4. LIPSCHITZ CONSTANT OF CONCATENATION

Lemma 4. Let $g : \mathbb{R}^n \rightarrow \mathbb{R}^m$ and $h : \mathbb{R}^p \rightarrow \mathbb{R}^q$ be functions with Lipschitz constant $\text{Lip}(g)$ and $\text{Lip}(h)$ respectively. Define $f : \mathbb{R}^{n+p} \rightarrow \mathbb{R}^{m+q}$ as the concatenation of g and h , that is $f(\mathbf{x}, \mathbf{y}) = (g(\mathbf{x}), h(\mathbf{y}))$. Then

$$\text{Lip}(f) \leq \sqrt{\text{Lip}(g)^2 + \text{Lip}(h)^2}.$$

Proof.

$$\begin{aligned} \|f(\mathbf{x}_1, \mathbf{y}_1) - f(\mathbf{x}_2, \mathbf{y}_2)\|_2^2 &= \left\| \begin{pmatrix} g(\mathbf{x}_1) - g(\mathbf{x}_2) \\ h(\mathbf{y}_1) - h(\mathbf{y}_2) \end{pmatrix} \right\|_2^2 \\ &= \|g(\mathbf{x}_1) - g(\mathbf{x}_2)\|_2^2 + \|h(\mathbf{y}_1) - h(\mathbf{y}_2)\|_2^2 \\ &\leq \text{Lip}(g)^2 \|\mathbf{x}_1 - \mathbf{x}_2\|_2^2 + \text{Lip}(h)^2 \|\mathbf{y}_1 - \mathbf{y}_2\|_2^2 \\ &\leq \text{Lip}(g)^2 (\|\mathbf{x}_1 - \mathbf{x}_2\|_2^2 + \|\mathbf{y}_1 - \mathbf{y}_2\|_2^2) + \text{Lip}(h)^2 (\|\mathbf{x}_1 - \mathbf{x}_2\|_2^2 + \|\mathbf{y}_1 - \mathbf{y}_2\|_2^2) \\ &= (\text{Lip}(g)^2 + \text{Lip}(h)^2) \left\| \begin{pmatrix} \mathbf{x}_1 - \mathbf{x}_2 \\ \mathbf{y}_1 - \mathbf{y}_2 \end{pmatrix} \right\|_2^2 \end{aligned}$$

where we used the definition of the ℓ_2 norm in the second and last line.

C.2. Lipschitz constant of Fourier feature encoding

We define the random Fourier feature encoding $\gamma : \mathbb{R}^d \rightarrow \mathbb{R}^{2m}$ as

$$\gamma(\mathbf{x}) = \begin{pmatrix} \cos(2\pi B\mathbf{x}) \\ \sin(2\pi B\mathbf{x}) \end{pmatrix}$$

where $B \in \mathbb{R}^{m \times d}$.

Proposition 3. *The Lipschitz constant of $\gamma(\mathbf{x})$ is bounded by*

$$\text{Lip}(\gamma) \leq \sqrt{8\pi}\|B\|.$$

Proof. Define $\mathbf{u}(\mathbf{x}) = \cos(2\pi B\mathbf{x})$ and $\mathbf{v}(\mathbf{x}) = \sin(2\pi B\mathbf{x})$. By definition of the Lipschitz constant and applying Lemma 1 we have

$$\begin{aligned} \text{Lip}(\gamma) &= \sup_{\mathbf{x}} \|\nabla\gamma(\mathbf{x})\| \\ &= \sup_{\mathbf{x}} \left\| \begin{pmatrix} \nabla \cos(2\pi B\mathbf{x}) \\ \nabla \sin(2\pi B\mathbf{x}) \end{pmatrix} \right\| \\ &= \sup_{\mathbf{x}} \left\| \begin{pmatrix} \nabla \mathbf{u}(\mathbf{x}) \\ \nabla \mathbf{v}(\mathbf{x}) \end{pmatrix} \right\| \\ &\leq \sup_{\mathbf{x}} \sqrt{\|\nabla \mathbf{u}(\mathbf{x})\|^2 + \|\nabla \mathbf{v}(\mathbf{x})\|^2} \\ &\leq \sqrt{\sup_{\mathbf{x}} \|\nabla \mathbf{u}(\mathbf{x})\|^2 + \sup_{\mathbf{x}} \|\nabla \mathbf{v}(\mathbf{x})\|^2}. \end{aligned}$$

The derivative of \mathbf{u} is given by

$$\begin{aligned} (\nabla \mathbf{u}(\mathbf{x}))_{ij} &= \frac{\partial u_i(\mathbf{x})}{\partial x_j} \\ &= \frac{\partial}{\partial x_j} \cos(2\pi \mathbf{b}_i^T \mathbf{x}) \\ &= -2\pi b_{ij} \sin(2\pi \mathbf{b}_i^T \mathbf{x}) \\ &= -2\pi b_{ij} v_i(\mathbf{x}), \end{aligned}$$

where \mathbf{b}_i corresponds to the i th row of B . We can write this more compactly as $\nabla \mathbf{u}(\mathbf{x}) = -2\pi \text{diag}(\mathbf{v}(\mathbf{x}))B$. A similar calculation for $\mathbf{v}(\mathbf{x})$ shows that $\nabla \mathbf{v}(\mathbf{x}) = 2\pi \text{diag}(\mathbf{u}(\mathbf{x}))B$.

All that remains is then to calculate the norms $\|\nabla \mathbf{u}(\mathbf{x})\|$ and $\|\nabla \mathbf{v}(\mathbf{x})\|$. Using submultiplicativity of the spectral norm we have

$$\begin{aligned} \sup_{\mathbf{x}} \|\nabla \mathbf{u}(\mathbf{x})\| &= \sup_{\mathbf{x}} 2\pi \|\text{diag}(\mathbf{v}(\mathbf{x}))B\| \\ &\leq \sup_{\mathbf{x}} 2\pi \|\text{diag}(\mathbf{v}(\mathbf{x}))\| \|B\| \\ &= 2\pi \|B\|, \end{aligned}$$

where we used the fact that the spectral norm of diagonal matrix is equal to its largest entry and that $|v_i(\mathbf{x})| \leq 1$ for all i . Similar reasoning gives $\sup_{\mathbf{x}} \|\nabla \mathbf{v}(\mathbf{x})\| = 2\pi \|B\|$. Finally we obtain

$$\begin{aligned} \text{Lip}(\gamma) &\leq \sqrt{\sup_{\mathbf{x}} \|\nabla \mathbf{u}(\mathbf{x})\|^2 + \sup_{\mathbf{x}} \|\nabla \mathbf{v}(\mathbf{x})\|^2} \\ &\leq \sqrt{(2\pi \|B\|)^2 + (2\pi \|B\|)^2} \\ &= \sqrt{8\pi} \|B\|. \end{aligned}$$

C.3. Lipschitz constant of set discriminator

The set discriminator $D : \mathbb{R}^{n \times (d+k)} \rightarrow [0, 1]$ is defined by

$$D(\mathbf{s}) = \rho \left(\frac{1}{\sqrt{n}} \sum_{i=1}^n \varphi(\gamma_x(\mathbf{x}_i), \gamma_y(\mathbf{y}_i)) \right),$$

where $\mathbf{s} = \{(\mathbf{x}_i, \mathbf{y}_i)\}_{i=1}^n \in \mathbb{R}^{n \times (d+k)}$ is treated as a fixed vector and each $\mathbf{x}_i \in \mathbb{R}^d$ and $\mathbf{y}_i \in \mathbb{R}^k$. The Fourier feature encodings for \mathbf{x}_i and \mathbf{y}_i are given by functions $\gamma_x : \mathbb{R}^d \rightarrow \mathbb{R}^{2m_x}$ and $\gamma_y : \mathbb{R}^k \rightarrow \mathbb{R}^{2m_y}$ respectively. The function $\varphi : \mathbb{R}^{2(m_x+m_y)} \rightarrow \mathbb{R}^p$ maps coordinates and features to an encoding of dimension p . Finally $\rho : \mathbb{R}^p \rightarrow [0, 1]$ maps the encoding to the probability of the sample being real.

Proposition 4. *The Lipschitz constant of the set discriminator D is bounded by*

$$\text{Lip}(D) \leq \text{Lip}(\rho)\text{Lip}(\varphi)\sqrt{\text{Lip}(\gamma_x)^2 + \text{Lip}(\gamma_y)^2}.$$

Proof. Write

$$\begin{aligned} D(\mathbf{s}) &= \rho\left(\frac{1}{\sqrt{n}}\sum_{i=1}^n \varphi(\gamma_x(\mathbf{x}_i), \gamma_y(\mathbf{y}_i))\right) \\ &= \rho(\eta(\mathbf{s})) \end{aligned}$$

where $\eta(\mathbf{s}) = \frac{1}{\sqrt{n}}\sum_{i=1}^n \varphi(\gamma_x(\mathbf{x}_i), \gamma_y(\mathbf{y}_i))$. Then we have

$$\text{Lip}(D) \leq \text{Lip}(\rho)\text{Lip}(\eta).$$

We can further write

$$\begin{aligned} \eta(\mathbf{s}) &= \frac{1}{\sqrt{n}}\sum_{i=1}^n \varphi(\gamma_x(\mathbf{x}_i), \gamma_y(\mathbf{y}_i)) \\ &= \frac{1}{\sqrt{n}}\sum_{i=1}^n \theta(\mathbf{s}_i), \end{aligned}$$

where $\mathbf{s}_i = (\mathbf{x}_i, \mathbf{y}_i)$ and $\theta(\mathbf{s}_i) = \varphi(\gamma_x(\mathbf{x}_i), \gamma_y(\mathbf{y}_i))$. By Lemma 3 we have

$$\text{Lip}(\eta) \leq \frac{1}{\sqrt{n}}\sqrt{n}\text{Lip}(\theta) = \text{Lip}(\theta).$$

We can then write

$$\begin{aligned} \theta(\mathbf{s}_i) &= \varphi(\gamma_x(\mathbf{x}_i), \gamma_y(\mathbf{y}_i)) \\ &= \varphi(\psi(\mathbf{s}_i)) \end{aligned}$$

where $\psi(\mathbf{s}_i) = (\gamma_x(\mathbf{x}_i), \gamma_y(\mathbf{y}_i))$. We then have, using Lemma 4

$$\text{Lip}(\theta) \leq \text{Lip}(\varphi)\text{Lip}(\psi) \leq \text{Lip}(\varphi)\sqrt{\text{Lip}(\gamma_x)^2 + \text{Lip}(\gamma_y)^2}.$$

Putting everything together we finally obtain

$$\text{Lip}(D) \leq \text{Lip}(\rho)\text{Lip}(\varphi)\sqrt{\text{Lip}(\gamma_x) + \text{Lip}(\gamma_y)}.$$

D. Additional results

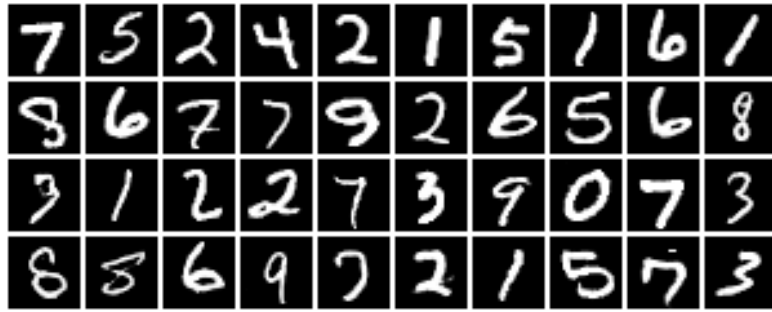


Figure 14. Additional MNIST samples.



Figure 15. Additional CelebAHQ 64 × 64 samples.



Figure 16. Additional CelebAHQ 128 × 128 samples.

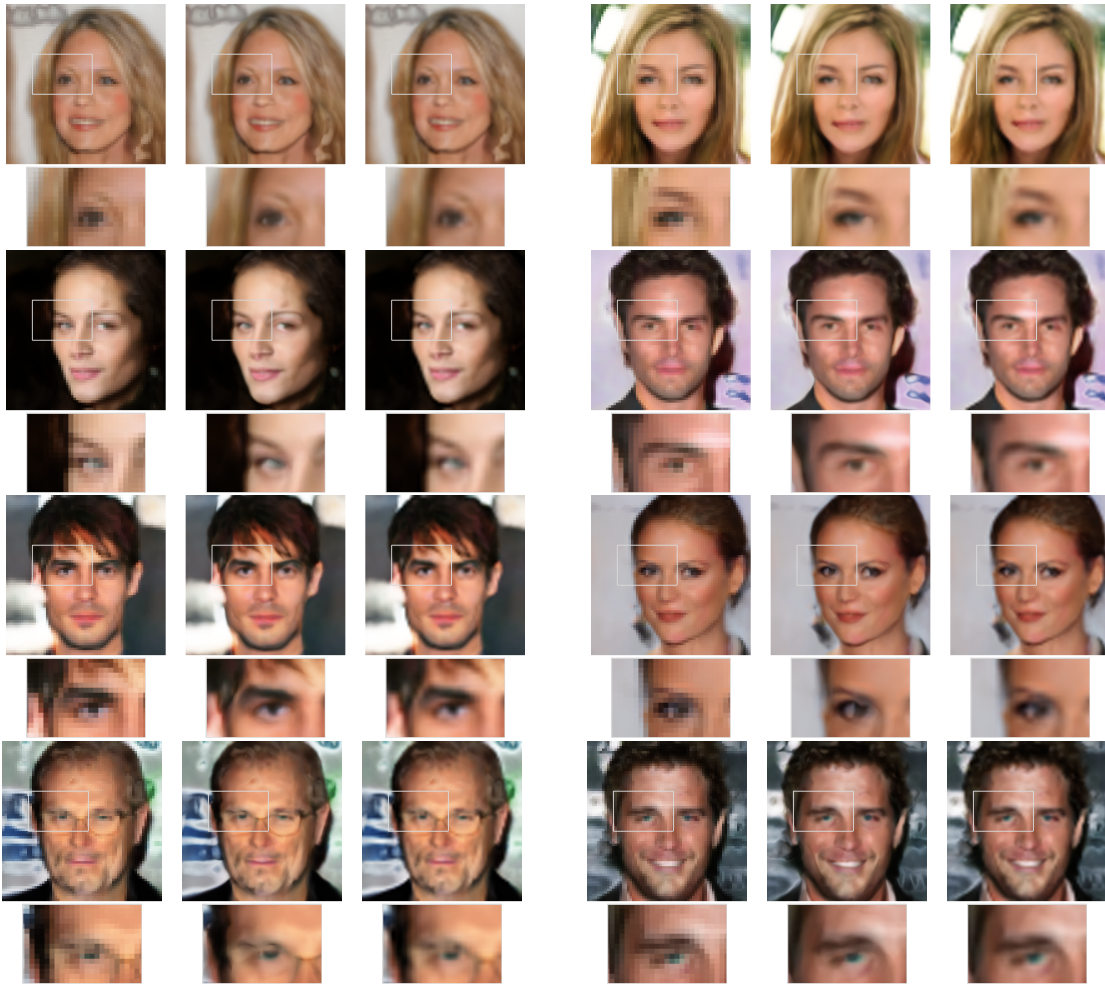


Figure 17. Additional superresolution samples. Left column shows superresolution from $64 \times 64 \rightarrow 256 \times 256$ and right column shows superresolution from $64 \times 64 \rightarrow 512 \times 512$



Figure 18. Additional Shapenet chairs samples.